processes

MDPI

Article

Finite Element Analysis on Inclusion Migration during Hot-Rolling Process of Ultralow Carbon Steel

Yanbin Yin * and Jiongming Zhang

State Key Laboratory of Advanced Metallurgy, University of Science and Technology Beijing, Beijing 100083, China
* Correspondence: ustbyby@ustb.edu.cn

Abstract: Slivers on the surface of rolled plates, which are serious defects for interstitial-free (IF) steel, occur mainly as a result of inclusions in continuous casting (CC) slabs. It is, therefore, important to study inclusions in CC slabs in terms of their migration towards the surface during hot rolling. To investigate inclusion migration during the hot rolling of ultralow carbon steel, a 3D numerical model was constructed using the finite element method. The positions of the inclusions in the surface layer of an IF steel slab (50 mm) were tracked during hot rolling using a node-tracking method. Furthermore, the study analyzed the effects of scarfing on inclusion migration during hot rolling and inclusion distribution in a hot-rolled plate. During the hot-rolling process, inclusions in the wide faces of the intermediate slab gradually migrated to the surface of the intermediate slab. Owing to a thickness reduction, accumulation areas of inclusions were finally generated at the edge of the hot-rolled plate; these areas may lead to sliver defects. The scarfing of the slab did not affect the distribution of inclusions in the hot-rolled plate; however, it may have reduced the inclusion content in the outermost layers of the hot-rolled plate. The inclusions were mainly located within 1 mm underneath the hot-rolled plate. Moreover, the inclusions near the inner arc of the CC slab were concentrated within 1.5 mm of the upper plate surface. Using galvanostatic electrolysis, the number of large inclusions in samples prepared from a hot-rolled plate obtained from a plant was measured. The measurements agreed well with the numerical model predictions, which validated the FE model in the current work.

Keywords: continuous casting slab; surface defect; inclusion migration; FE model; ultralow carbon steel

Citation: Yin, Y.; Zhang, J. Finite Element Analysis on Inclusion Migration during Hot-Rolling Process of Ultralow Carbon Steel. *Processes* **2023**, *11*, 934. https://doi.org/10.3390/pr11030934

Academic Editors: Peng Lan and Ligen Sun

Received: 3 January 2023
Revised: 14 March 2023
Accepted: 15 March 2023
Published: 18 March 2023

1. Introduction

Ultralow carbon steels, such as IF steel, are extensively used to produce cold-rolled sheets for use in automobiles and domestic appliances [1]. Excellent surface qualities are required for this category of steel grades [2,3]. The alleviation of the appearance of surface defects is of great importance for the production of ultralow carbon steels [4]. Among the surface defects present in ultralow carbon steel sheets, slivers and blisters resulting from the solidified shell entrapment of inclusions and slag entrainment that occur during CC are the most frequent and harmful [5–7]. In recent decades, significant efforts have been contributed to improving the cleanliness of molten steel and reducing inclusions in molten steel during steelmaking and CC processes [4,8–10]. Nevertheless, inclusions inevitably remain in slabs during CC [11–13]. Residual inclusions in the as-cast slabs can evolve into surface defects during rolling. Hence, research on the inclusion evolution that occurs during the rolling process is important in reducing surface defects and improving the surface quality of ultralow carbon steel products.

In recent years, some experimental studies [14–27] and numerical simulation works [27–45] have been conducted on the behavior of inclusions in steel during the rolling process. Experimental studies are generally conducted to evaluate the composition transformation [14,16,19,22] and deformability [14,16–18,20–25,27] of inclusions after rolling, as well as the generation

of voids surrounding the inclusions [14,17,18]. However, these experimental studies are mainly conducted through the methods of measuring the compositions and dimensions of the inclusions in steel samples before and after the rolling process. Hence, an intuitionistic understanding of the composition evolution and deformation process of inclusions during the rolling process is difficult to attain based on experimental investigations.

Numerical simulation works mainly focus on the stresses and strains of inclusions and the steel matrixes around them through the use of the finite element analysis (FEA) method. Luo and Ståhlberg [29,30] developed a two-dimensional (2D) rigid–viscoplastic finite element (FE) code to analyze the shape evolution of oxidized inclusions and MnS inclusions in steels during flat rolling. The effects of the rolling temperature, friction and rolling reduction on inclusion deformations were investigated using an FE model. An FE code was constructed by Ervasti and Ståhlberg [31] based on a commercial package to study void initiation close to a hypothetical single macroinclusion (with a radius of 4 mm) during the hot rolling of steel slabs. Using the numerical model, void formations around inclusions at different distances from the slab surface were analyzed for different single-pass reductions and roll radii. The results revealed that a roll with a large radius should be chosen to prevent the generation of voids. Furthermore, the threat of a void starting to form turned out to be slight for high reductions and in the vicinity of the slab surface. Yu et al. [36] studied the deformation behaviors of spherical inclusions in stainless steel strips during multipass cold rolling using a 3D FE method and updating the geometric method. It was pointed out that inclusions with a diameter of less than 10 μm could hardly deform. Cheng et al. [37–39] developed a 3D FE model to comprehensively investigate inclusion deformations and void formations for different inclusion compositions and steel grades. The effects of the rolling temperature, flow stresses of inclusions and steel matrix, reductions on void size and inclusion deformation abilities were analyzed. The critical temperatures above which no voids formed were different for different inclusions and steel grades. Apart from the FEA, some novel numerical methods have recently been proposed for the stress–strain analysis of isotropic and anisotropic media. Among them, the "differential quadrature" [46] and "Bezier" [47] methods proved to have a higher stability and accuracy than other numerical methods.

Slivers on the surface of rolled plates, which are serious defects for interstitial-free (IF) steel, occur mainly as a result of inclusions in CC slabs. To reduce sliver defects on rolled plates, the "scarfing" operation, which utilizes flame jets or mechanical grinding, has been adopted in some steel plants. Wang et al. [48] studied the inclusion distribution in surface layers of IF steel slabs with an original position analyzer (OPA); the results indicated that scarfing 3.5 mm from the top slab surface could improve the strip quality. Lee et al. [49] reported that large inclusions mainly appeared at 5–20 mm beneath the CC slab's surface. However, the sliver defects still often appeared on rolled plate produced using scarfed CC slabs. The scarfing depth and effectiveness of the scarfing operation are controversial. As a result, this operation has not been adopted in some steel plants.

The scope of this study was to investigate inclusion migration during the hot rolling of IF steel using a 3D FE model. The positions of inclusions in the surface layer of an IF steel slab were tracked during hot rolling using a node-tracking method. The distribution of inclusions in the hot-rolled plate was revealed. To reveal the effectiveness of the "scarfing" operation, the effects of scarfing on inclusion migration during hot rolling and on the inclusion distribution in hot-rolled plates were analyzed. With the method of galvanostatic electrolysis, large inclusions in samples prepared from a hot-rolled plate obtained from a steel plant were measured, and the validity of the FE model was confirmed.

2. Numerical Methodology

2.1. The Thermophysical Parameters

Based on the chemical compositions listed in Table 1, true stress–strain curves of IF steel were obtained for different strain rates and temperatures using the material property simulation package JMatPro (Version 7.0). As shown in Figure 1a, the true stress–strain

curves obtained using JMatPro were in good agreement with the curves obtained using Gleeble-1500D. Thus, the validity of the calculations could be confirmed. In addition, other material parameters (e.g., Young's modulus, Poisson's ratio and the thermal conductivity coefficient) were calculated using JMatPro, the results of which are shown in Figure 1b. These calculated parameters were fed into the simulation software Transvalor FORGE through the software interface; the subroutine codes of the setup of material properties can be found in the Appendix A.

Table 1. Chemical compositions of IF steel.

Element	C	Si	Mn	P	S	Al_t	Ti	N
%wt	≤0.003	≤0.03	0.11–0.15	≤0.012	≤0.01	0.02–0.045	0.05–0.09	≤0.004

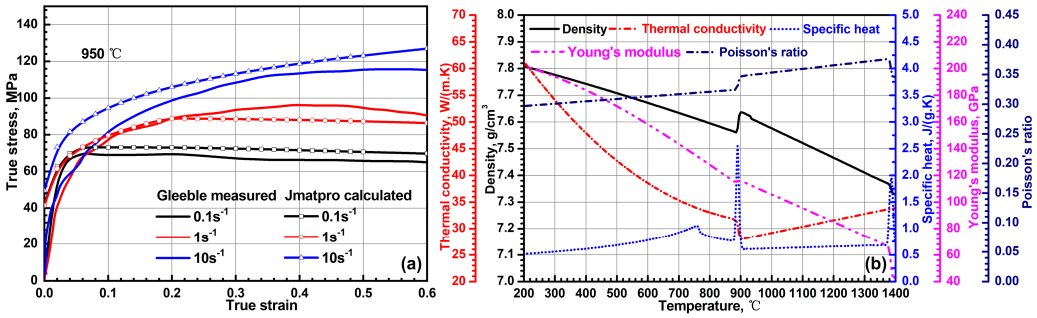

Figure 1. Thermophysical parameters of IF steel used in the calculation: stress–strain curves (**a**) and material parameter–temperature curves (**b**).

2.2. The Hot-Rolling Process Parameters

A 1580 mm hot-rolling production line of a steel plant was considered as the research object of the study. As shown in Figure 2, the 1580 mm hot-rolling production line was equipped with semicontinuous mills, including two reversible roughing mills (R1 and R2) and seven-strand finishing mills (F1–F7). Based on the IF steel rolling schedule used in the field production of the plant, a pass was conducted for the IF steel slab in the R1 roughing mill. Subsequently, the slab was reversibly rolled using five passes in the R2 roughing mill. Finally, seven continuous rolling passes were conducted in the finishing mill.

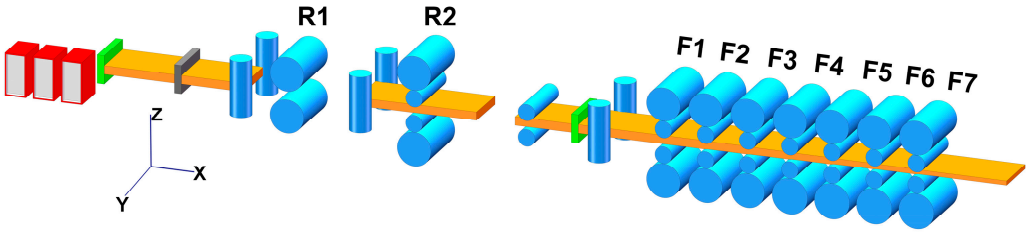

Figure 2. Schematic diagram of a 1580 mm hot-rolling production line.

To investigate the effect of surface scarfing on inclusion migration during hot rolling, calculations were performed for two cases: Case-1 and Case-2. In Case-1, a 1050 mm × 247 mm slab was not scarfed before it was rolled, whereas in Case-2, a 3 mm surface scarfing was conducted on the slab to obtain a cross-section of 1044 mm × 241 mm before it was rolled. The compression ratio of each pass in Case-1 was the same as that in Case-2. The rolling schedules (intermediate slab thicknesses after each pass) of the two cases are listed in Table 2. To reduce the calculation time and simulate the hot-rolling process to the maximum extent, the slab size in the rolling direction was set to 1500 mm.

Table 2. IF steel hot-rolling schedules with thicknesses of plates for two cases (unit: mm).

Cases	Before Rolling	R1 Roughing Mill	R2 Roughing Mill				
			R2-1	R2-2	R2-3	R2-4	R2-5
Case-1	247	172.9	124.49	92.12	70.01	54.61	45.63
Case-2	241	168.7	121.46	89.88	68.31	53.28	44.52
Cases	Finishing Mill						
	F1	F2	F3	F4	F5	F6	F7
Case-1	27.25	17.55	12.34	9.06	7.14	6.15	5.5
Case-2	26.59	17.12	12.04	8.84	6.97	6.01	5.37

2.3. The Solving and Numerical Details

The initial and boundary conditions used in the study were listed in Table 3. To compute the thermal–mechanical coupling of large deformations, the Euler–Lagrangian coupling algorithm of the FORGE package was used. A three-dimensional solid tetrahedron element with four nodes was adopted for the slab in the simulations.

Table 3. The initial and boundary conditions for the simulations.

Conditions	Parameters	Values	Notes
Initial conditions	Slab initial temperature	1210 °C	
	Slab initial velocity	$V_i < V_r$	V_i is initial velocity; V_r is rolling speed.
Boundary conditions	Ambient temperature	30 °C	
	Temperature of rollers	250 °C	
	Rotary speed of rollers	$\omega = V_r/R$	R is the roller radius.
	Contact heat transfer	$q_c = h(T - T_r)$	h is the coefficient of the contact heat transfer; T is the slab temperature; T_r is the roller temperature
	Radiant heat	$q_r = \sigma_{heat}\varepsilon_{heat}(T^4 - T_0^4)$	ε_{heat} is the emissivity; σ_{heat} is Stefan's constant; T_0 is the ambient temperature.
	Heat dissipates of plastic strain	$\dot{W} = \eta K_s\sqrt{3}\dot{\varepsilon}^{m+1}$	η is the strain efficiency; K_s is the constant; $\dot{\varepsilon}$ is the strain rate; m is the sensitivity coefficient of the strain rate.
	Friction heat	$q = b_1/(b_1 + b_2)\tau_{fr}V_g$	b_1 and b_2 are the ratios of the heat transferred from the friction interface to the slab and rollers; V_g is the sliding velocity; τ_{fr} is the shear friction.

As shown in Figure 3, the geometry model and grid structure were constructed for the R1 pass. Subsequently, a coupling calculation for the R1 pass was performed. After performing the R1 pass calculation, the geometry model and grid structure of the deformed intermediate slab with detailed thermal–mechanical information were constructed for the R2-1 pass. The R2-1 pass computation was performed thereafter. The R2-2 pass analysis was performed based on the R2-1 pass procedure, but assuming that the rotation of the rollers and the movement of the intermediate slab were in the opposite directions. The analysis of passes R2-3, R2-4 and R2-5 was also similarly performed. After simulating the R2-5 pass, the cell model of the deformed intermediate slab with detailed thermal–mechanical information was considered in the analysis of the continuous rolling process (F1–F7). Finally, the continuous rolling process was simulated, and the intermediate slab was deformed to obtain a hot-rolled plate 5.5 or 5.37 mm in thickness.

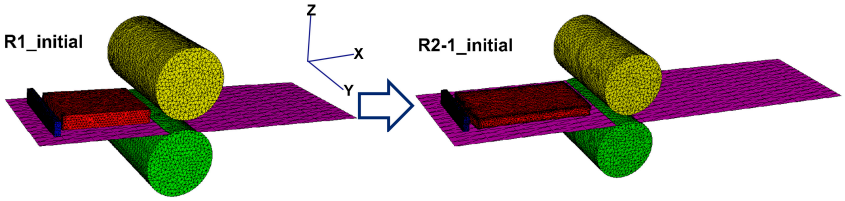

Figure 3. The geometry models and grid structures of the R1 and R2-1 passes.

In this study, inclusions in the intermediate slab were simplified using different points, as stated in Tripathy et al. [32]. The inclusion positions were tracked during the calculations using the sensor module of the FORGE package to reveal inclusion migration during the hot-rolling process. In practice, the inclusions exposed to the surface of the intermediate slab would be ground off by the rollers. Therefore, during the tracking process, inclusions that were within 0.1 mm of the upper and lower surfaces of the intermediate slab were considered to have been removed, and, thus, their positions were not tracked in the subsequent process.

The initial positions of the inclusions in the slab were determined using numerical simulations of the inclusion transport in the CC slab [50]. According to previous studies [50–52], large inclusions are mainly distributed within 50 mm beneath the inner and outer slab arcs. Therefore, in this study, only those inclusions were tracked during hot rolling. Figure 4 shows the initial distribution of inclusions in the CC slab before performing the FE calculations pertaining to hot rolling. To reduce the computational cost and accelerate the calculation process, only the inclusions in the slab that were 50 mm long in the casting (rolling) direction were tracked. In Case-2, due to surface scarfing, the inclusions within 3 mm beneath the CC slab were ignored and not tracked in the subsequent FE calculations. The study mainly focused on position migration in the slab during the hot-rolling process and along the thickness and width directions of the inclusions. The inclusion positions were projected on a cross-sectional plane in the discussion that follows (Figure 4b).

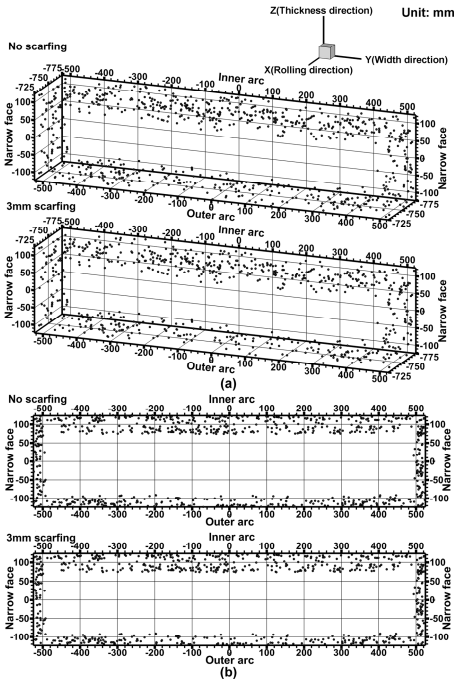

Figure 4. The initial positions of inclusions in the CC slab: 3D (**a**) and 2D (**b**) distributions.

A sensitivity analysis was conducted for different meshes, as shown in Figure 5. The coarse, medium and fine meshes consisted of approximately 90,000, 160,000 and 220,000 elements. The mesh had an effect on the results to some extent. As the number

of elements increased, the variation in the calculated results (equivalent strain and temperature) decreased. In the current work, a fine mesh for the slab with ~220,000 elements was selected.

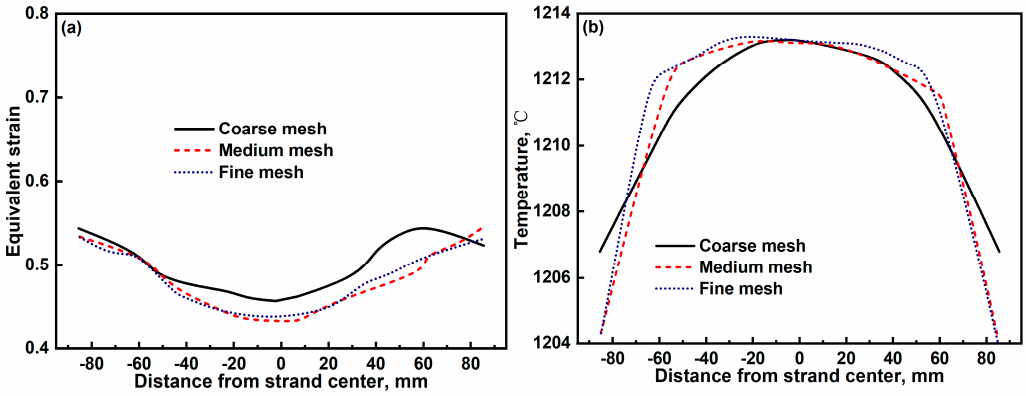

Figure 5. The variations in equivalent stains (**a**) and temperatures (**b**) along the thickness direction of the intermediate slab after R1 pass at three mesh levels.

3. Experimental Methodology

To investigate the distribution of inclusions in the hot-rolled plate and validate the FE model that was constructed, large inclusions (>50 μm) in the hot-rolled plate were quantitatively extracted using galvanostatic electrolysis as Figure 6a shows [50]. The pH of the electrolyte was ~7. The current density was ~15 mA·cm^{-2}. Figure 6b presents the machining process of the steel samples obtained using galvanostatic electrolysis. Samples were taken from the centers and edges of hot-rolled plates from a steel plant. Four samples, namely, E1–E4, which were 100 and 15 mm long in the width and rolling directions, respectively, were obtained from the edge of the hot-rolled plates. Each sample was divided into five equal parts along the thickness direction of the plate (e.g., E1.1–E1.5). E1.1, E2.1, E3.1 and E4.1 were, thereafter, spot welded to obtain a sample, representing the uppermost position (0–1 mm beneath the upper surface or the inner arc) of the edge of the hot-rolled plate for use in the galvanostatic electrolysis. Similarly, nine other samples representing different positions of the hot-rolled plate produced from a slab that had no scarfing were prepared. Samples of the hot-rolled plate scarfed before rolling were similarly prepared for use in the galvanostatic electrolysis.

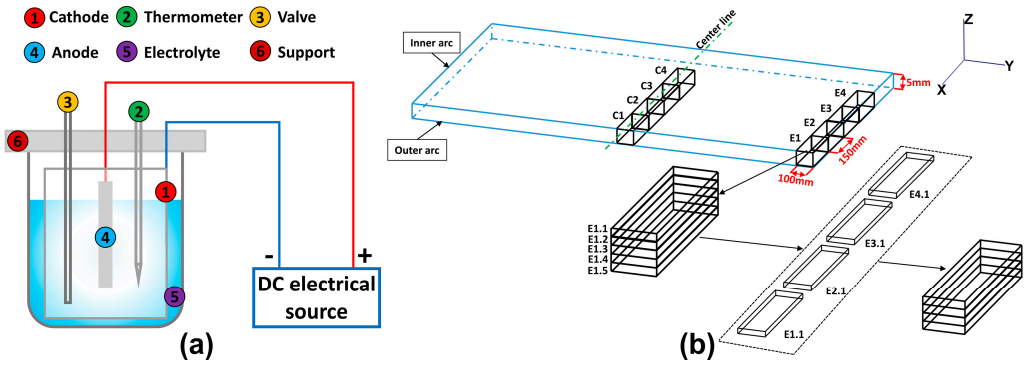

Figure 6. Schematic diagram for galvanostatic electrolysis method (**a**) and sample machine process (**b**).

4. Results and Discussion

4.1. Prediction of Inclusion Migration during the Roughing Rolling Process

Figure 7 shows the distributions of the inclusions in the intermediate slabs after the R1 pass. In terms of the inclusion distributions, there was no obvious difference between the slab before rolling and the intermediate slab after the R1 pass. Nevertheless, after the R1 pass, the inclusions in the slabs became concentrated. Furthermore, after the R1 pass, no

apparent difference could be observed between the inclusion distribution in the slab with no scarfing and in the slab with 3 mm scarfing.

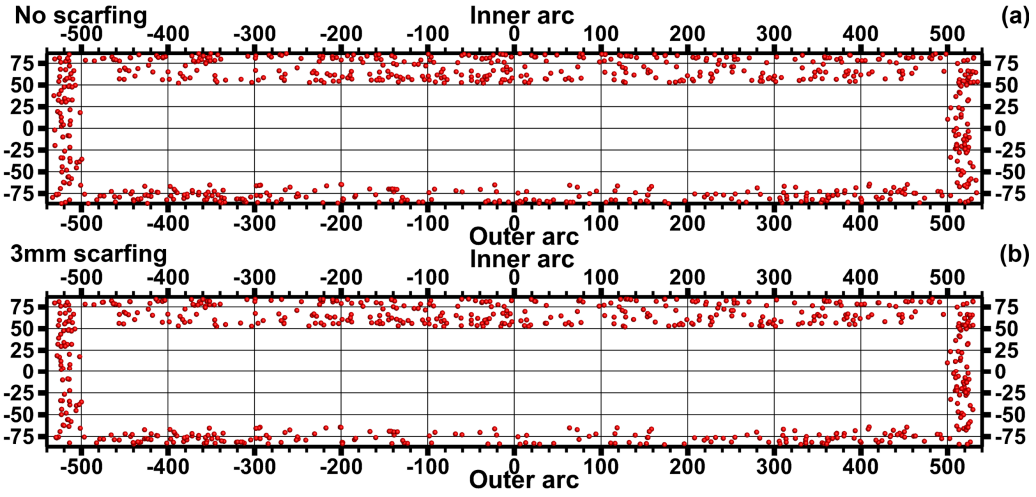

Figure 7. The distribution of inclusions in the intermediate slab after R1 pass: the case without scarfing (**a**) and the case with 3 mm scarfing (**b**).

Figure 8 shows the evolution of the inclusion distributions in the intermediate slabs during the R2 rough rolling process (R2-1 to R2-5 passes). Some characteristics of inclusion distribution evolution could be observed during the R2 rough rolling process. First, the inclusions near the wide faces of the intermediate slab became increasingly dense and moved close to the surface. Second, the inclusions in the accumulation zone of the intrusions located in the inner arc of the intermediate slab (at approximately 1/4th of the thickness) gradually migrated to the inner arc surface. Third, as rolling continued, the difference between the inclusion distribution in the slab that was not scarfed and in the slab with 3 mm scarfing became increasingly small. Additionally, accumulation zones of inclusions were generated near the narrow face of the intermediate slab. These accumulation zones of inclusions resulted from the size reduction in the intermediate slab along its thickness direction during the rolling process.

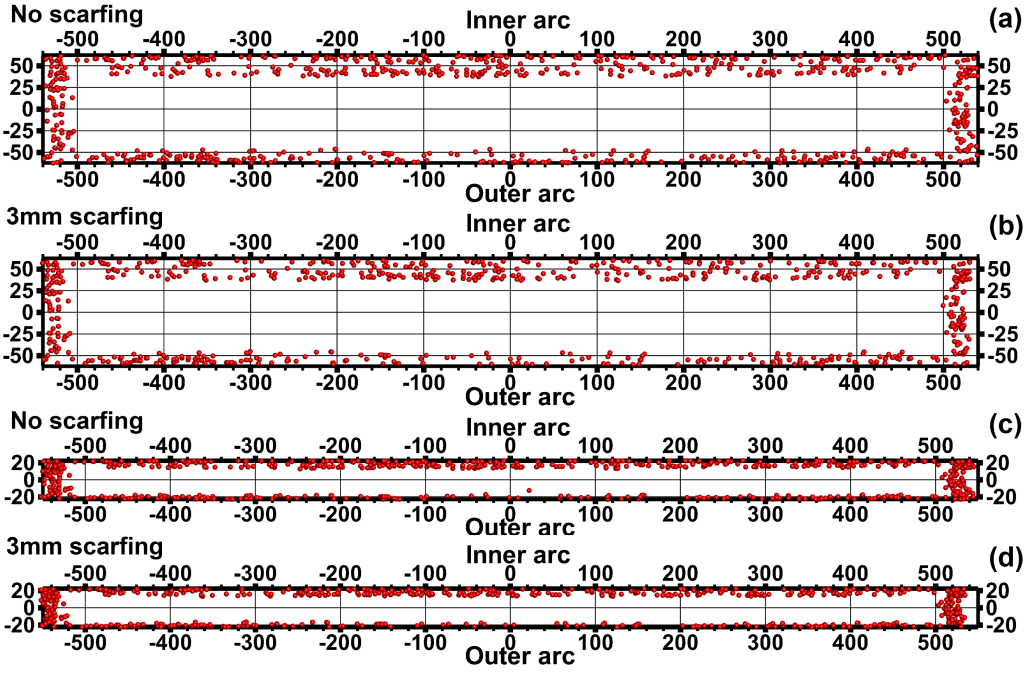

Figure 8. The distributions of inclusions in the intermediate slab after R2-1 pass (**a**,**b**) and R2-5 pass (**c**,**d**).

4.2. Statistics of Inclusion Distribution in the Intermediate Slab during the Roughing Rolling Process

The prediction results shown in Figures 7 and 8 demonstrate the evolution of the inclusion distribution in the intermediate slabs during the rolling process. However, these two figures can only merely present the inclusion distributions on the cross-sections of the intermediate slabs. The variations in inclusion contents along the thickness direction on the cross-section of the intermediate slab after different passes could be useful in determining inclusion migration in the slabs during the rolling process. Hence, it was necessary to reveal the statistical results for the variations in inclusion positions on the cross-section of the intermediate slab after different passes based on the numerical simulations. To observe the statistical regularities of inclusion position evolutions during the rolling process, each intermediate slab was divided into 50 layers along its thickness direction. The number of inclusions in each layer was counted and the proportion of inclusions in each layer was calculated after each pass.

Figure 9 shows the inclusion distributions along the thickness directions in the two cases considered before and after the R1 pass. In the slab with no scarfing, the number of inclusions that were farther away from the wide face of the intermediate slab decreased after the R1 pass. Nevertheless, the inclusions near the wide face of the slab increased in number after the R1 pass. In other words, the inclusions in the slab tended to migrate from inside to the wide face during the R1 pass. The number of inclusions in the layer closest to the outer arc face also increased after the R1 pass. However, the number of inclusions in the layer closest to the inner arc face decreased after the R1 pass. During the R1 pass, some inclusions migrated to the outermost layer of the slab; meanwhile, some inclusions in the outermost layer were removed by the roller. The inclusion migration trend in the slab with 3 mm scarfing during the R1 pass was also observed. The number of inclusions in the surface layer of the slab decreased and the number of inclusions in the outermost layer of the scarfed slab increased after the R1 pass.

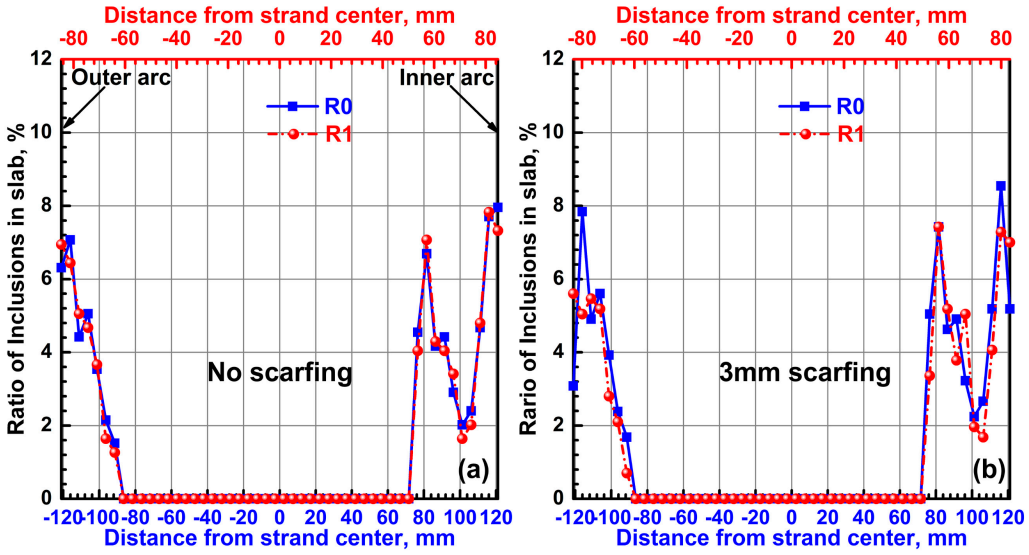

Figure 9. The inclusion distributions along the thickness direction before and after the R1 pass: the case without scarfing (**a**) and the case with 3 mm scarfing (**b**).

Figure 10 shows the inclusion distributions in the two slabs along their thickness directions before and after the R2-5 pass. The inclusion positions in the intermediate slab migrated steadily during the R2 hot-rolling process. The inclusions inside the slab gradually migrated to the surface. Consequently, the proportion of inclusions inside the intermediate slabs decreased as the hot-rolling process continued. In addition, during the R2 hot-rolling process, the inclusion accumulation zones located in the inner arc of the intermediate slabs moved close to the inner arc surfaces. Moreover, in the slab with no scarfing and in the slab

with 3 mm scarfing, the inclusion distribution trends along the thickness directions were similar. Nevertheless, because the slab surface was scarfed before starting the hot-rolling process, the number of inclusions in the outermost layer of the intermediate slab for the case with 3 mm scarfing was less than that of the case without scarfing after the R2-5 pass, which was similar to the situation after the R1 pass.

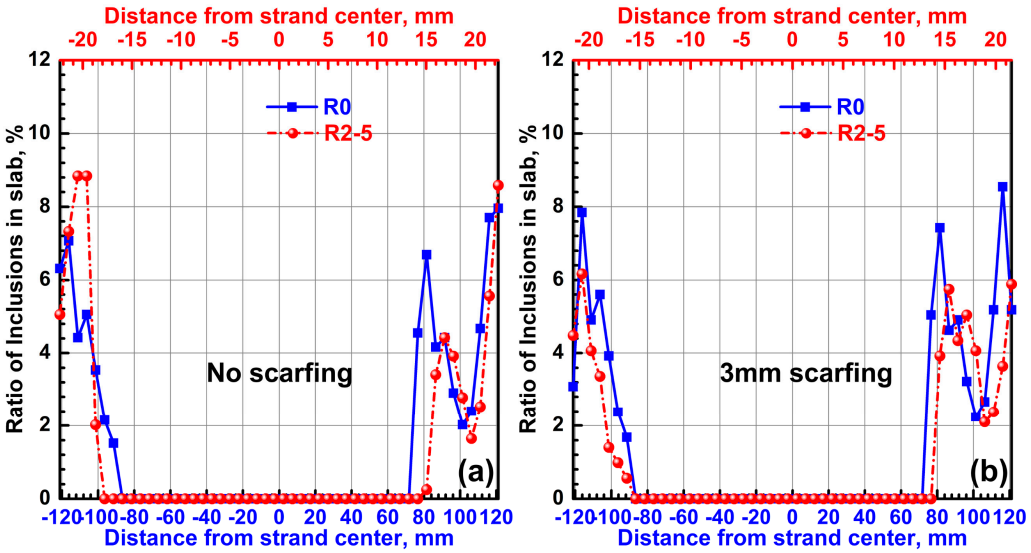

Figure 10. The inclusion distributions along the thickness direction before and after the R2-5 pass: the case without scarfing (**a**) and the case with 3 mm scarfing (**b**).

Figure 11 shows the distribution of the equivalent strain in the intermediate slabs along the thickness direction after each pass. During each pass, the equivalent strain in the surface layer of each slab was larger than that inside the slab. For the initial R1 pass, the equivalent strain variation was the most obvious. It was precisely because of the equivalent strain distribution along the thickness direction of the intermediate slab that the inclusions in the slab interior migrated to the surface layer during the hot-rolling process.

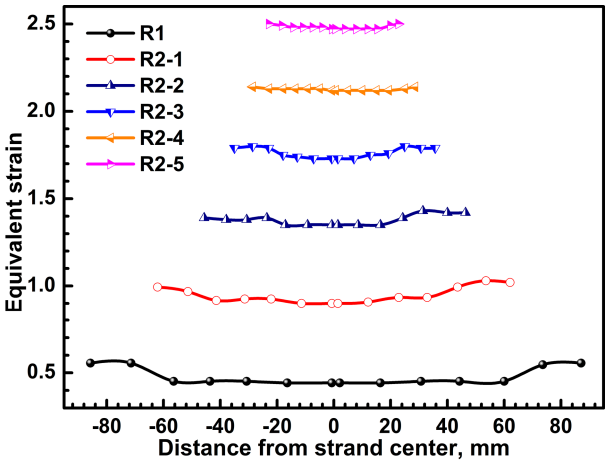

Figure 11. Variations in equivalent strain in the intermediate slab along the thickness direction.

4.3. Prediction and Measurement of Inclusion Distribution in the Hot-Rolled Plate

Figure 12 shows the distributions of the inclusions in the hot-rolled plate after rolling was completed. The inclusions were located almost within 1 mm beneath the surface of the hot-rolled plate. Furthermore, the distribution of inclusions in the hot-rolled plate in the case with no scarfing was similar to that in the case with 3 mm scarfing. In other words, scarfing hardly influenced the inclusion distribution in the intermediate slab or hot-rolled

plate during the hot-rolling process. In addition, owing to the thickness reduction, the inclusions near the narrow face of the intermediate slab gradually accumulated along the thickness direction as the hot-rolling process continued. Finally, accumulation areas of inclusions were generated at the edge of the hot-rolled plate, where sliver defects of the rolled plate often appeared.

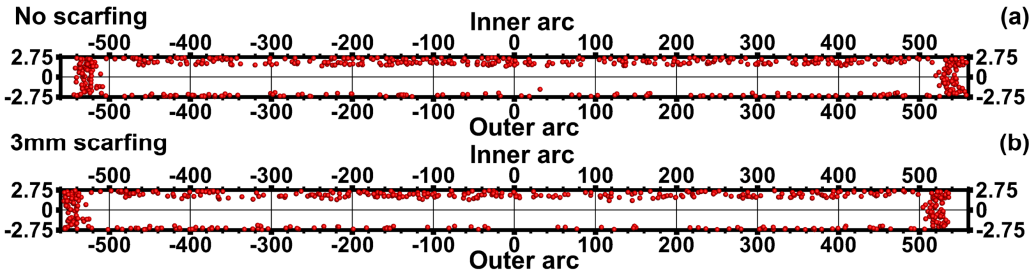

Figure 12. The distributions of inclusions in the hot-rolled plate after finishing rolling: the case without scarfing (**a**) and the case with 3 mm scarfing (**b**).

Figure 13a shows the inclusion distribution along the thickness direction of the hot-rolled plate calculated using the proposed FE model. For the two cases with no scarfing and with 3 mm scarfing, the prediction results showed that inclusions were mainly located within 1 mm beneath the underside (outer arc) of the hot-rolled plate. Moreover, inclusions near the inner arc of the CC slab were concentrated within 1.5 mm beneath the upper surface of the plate after the hot-rolling process was completed. In addition, the number of inclusions in the outermost layers of the plate in the case with 3 mm scarfing was less than that in the case without scarfing. Hence, the scarfing of the CC slab did not affect the distribution of inclusions in the hot-rolled plate; nevertheless, it could reduce the inclusion content in the outermost layers of the hot-rolled plate. The research object of this study was endogenous inclusions and not external inclusions. External inclusions, particularly inclusions generated by mold flux entrainment, which are typically large and prone to be captured in the initial solidified mold shell, are generally located in the region extremely close to the CC slab's surface. Therefore, CC slab scarfing can effectively reduce the surface defects of hot-rolled plates caused by mold flux entrainment. Nevertheless, slag entrainment in the mold typically occurs under unsteady casting conditions (e.g., the initial casting stage, casting speed change, nozzle change and ladle change). Hence, scarfing may have little effect on reducing surface defects in plates produced from normal CC slabs.

Figure 13b shows the measured inclusion distributions of the hot-rolled plate along the thickness direction in the width center and edge regions. As already mentioned, the inclusions near the narrow face of the CC slab gradually accumulated along its thickness direction as the hot-rolling process continued. Thus, the number of inclusions within the edge region of the hot-rolled plate was greater than in its center region. In the width center region of the plate, the inclusions were mainly concentrated within 1 mm beneath the lower surface of the plate and 2 mm beneath the upper surface of the plate. Furthermore, no inclusions were detected within the width center region of the plate. The measurements of the inclusion distribution in the hot-rolled plate agreed well with the numerical model predictions, which also validated the FE model used in the study. Figure 13c shows the morphology of a sliver defect in a hot-rolled IF steel plate obtained from the production field. As stated above, the inclusions in the edge region of the intermediate slab gradually concentrated along the thickness direction of the slab during its hot rolling. Consequently, concentrated zones of inclusions appeared in the edge region of the hot-rolled plate, which can produce sliver defects.

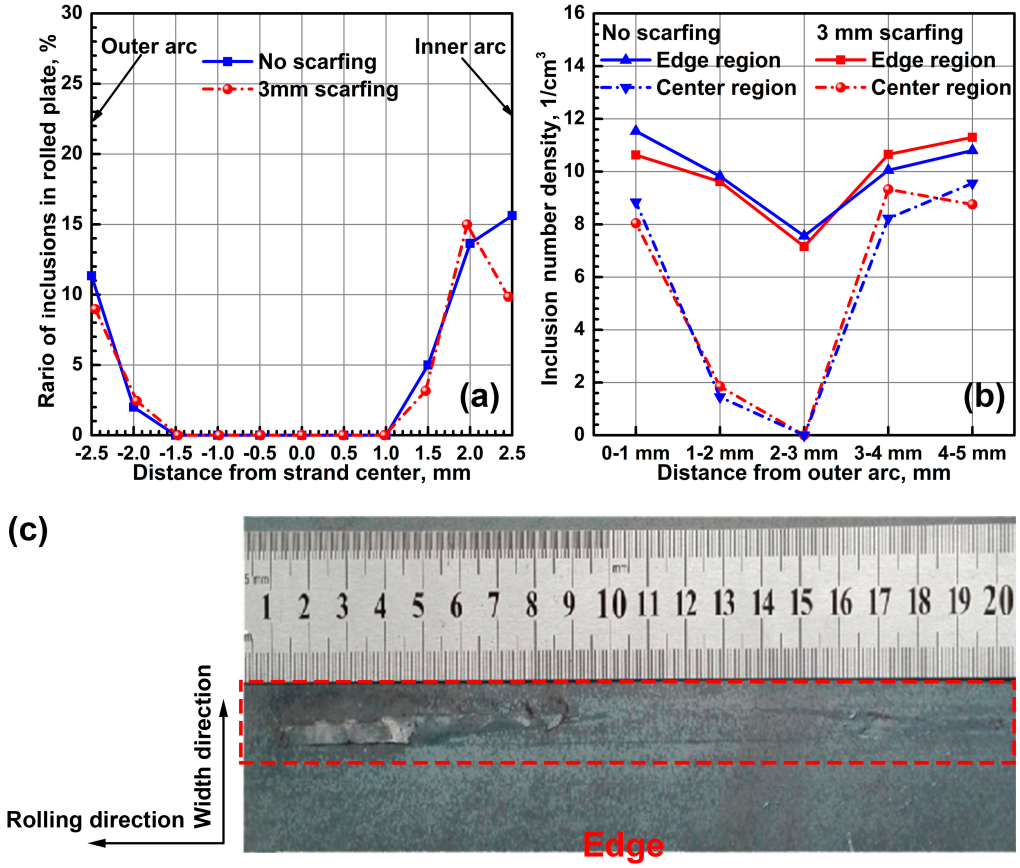

Figure 13. The distributions of inclusions along the thickness of the hot-rolled plate: the predicted results (**a**) and the measured results (**b**); the sliver defect of the hot-rolled plate (**c**).

5. Conclusions

In this study, a 3D numerical model using the finite element method was constructed to simulate the hot rolling of IF steel. The inclusion positions in the IF steel slab surface layer were tracked during the hot-rolling process using a node-tracking method. The distribution of inclusions in the hot-rolled plate was also observed. The study revealed the effect of scarfing on inclusion migration during hot rolling and inclusion distribution in a hot-rolled plate. Using galvanostatic electrolysis, measurements of large inclusions in samples obtained from hot-rolled plates in a plant were performed, which verified the validity of the FE model. The study conclusions are as follows:

1. During the hot-rolling process, inclusions in the wide faces of intermediate slabs gradually migrated to the surfaces. Moreover, inclusions in the accumulation zone located in the inner arc of the intermediate slabs were close to the inner arc surfaces. During the hot-rolling process, equivalent strains in the surface layers of the slabs were larger than the equivalent strains inside the slabs, which caused the inclusions inside the slabs to migrate to the surface layer.
2. As the hot-rolling process continued, the difference between the inclusion distributions in the slab with no scarfing and in the slab with 3 mm scarfing decreased significantly. For the two cases, the inclusions were mainly located within 1 mm underneath the hot-rolled plate. Moreover, the inclusions near the inner arc of the CC slab were concentrated within 1.5 mm of the upper plate surface. The scarfing of the CC slab did not affect the inclusion distribution in the hot-rolled plate; nevertheless, it may have reduced the inclusion content in the outermost layer of the plate.
3. Due to the reduction in the intermediate slab's thickness, the inclusions near the narrow face of each CC slab gradually accumulated in its thickness direction as the

hot-rolling process continued. Finally, accumulated areas of inclusions were generated at the edge of the hot-rolled plate, which could have caused sliver defects.

4. To experimentally investigate the inclusion distribution in a hot-rolled plate and validate the FE model that was constructed, large inclusions in the hot-rolled plate obtained from a steel plant were quantitatively extracted using galvanostatic electrolysis. The measurements of the inclusion distribution in the hot-rolled plate agreed well with the numerical model predictions, thereby validating the FE model constructed in the study.
5. Owing to the computing capacity of the computer and the maturity of the numerical model, some works could not be conducted in the current stage. These works, such as a coupling model between inclusions in the microscale and steel matrixes in the macroscale, modeling on the breakup of inclusions in steel matrixes during the rolling process, the effect of adhesion between inclusions and the steel matrix on the inclusion deformation during the rolling process, should be performed in the future.

Author Contributions: Y.Y. and J.Z. conceived and designed the study; Y.Y. performed the numerical calculations; Y.Y. conducted the experiments; Y.Y. and J.Z. wrote the paper. All authors have read and agreed to the published version of the manuscript.

Funding: This research was funded by the National Natural Science Foundation of China (nos. 52104320 and 51834002) and the Postdoctoral Research Foundation of China (no. 2021M690371).

Institutional Review Board Statement: Not applicable.

Informed Consent Statement: Not applicable.

Data Availability Statement: The data presented in this study are available on request from the corresponding author. The data are not publicly available due to privacy restrictions.

Conflicts of Interest: The authors declare no conflict of interest.

Appendix A

The subroutine codes of the setup of material properties in the numerical simulations are as follows:

```
{Software= GLPre_V2.1}
{Supported_Software= FORGE2 FORGE3}
{Comments=
ALLOY_ID_WT% 0.041C0.003Cr0.01Fe99.7243Mn0.11N0.0017Ni0.01P0.012S0.008Si0.03Ti0.05
ALLOY_ID_AT% Al0.084C0.013Cr0.011Fe99.61Mn0.11N0.007Ni0.01P0.022S0.014Si0.06Ti0.058
Alloy calculated with JMatPro
JMatPro VERSION 7.0.0
MATERIAL TYPE = General Steel
RT STRENGTH INPUT = 0.2% Proof Stress 1000 MPa / 145.05 ksi
}
{Rheological_Units= mm-mpa}
{Rheological_Data_as_Text= EVP
Thermoecroui: Pointapoint, File = IF_properties_FlowStress.dat
DatAJMatpro = IF_properties_PhysProps.dat}
{External_Files_To_Copy=IF_properties_FlowStress.dat, IF_propties_PhysProps.dat}
{Thermal_Units= SI}
{Thermal_Data_as_Text=
!Thermal coefficients Define in DataJMatpro
Epsilon = 0.88 ! Emissivity}
```

References

1. Yang, W.; Zhang, L.; Wang, X.; Ren, Y.; Liu, X.; Shan, Q. Characteristics of Inclusions in Low Carbon Al-Killed Steel during Ladle Furnace Refining and Calcium Treatment. *ISIJ Int.* **2013**, *53*, 1401–1410. [CrossRef]
2. Sengo, S.; Romano Triguero, P.; Zinngrebe, E.; Mensonides, F. Tracing the Origin of Non-ferrous Oxides in Lamination Defects on Hot-Rolled Coils: Mold Slag Entrainment vs Submerged Entry Nozzle Reaction Products. *Metall. Mater. Trans. B* **2017**, *48*, 1690–1702. [CrossRef]
3. Ji, Y.; Liu, C.; Lu, Y.; Yu, H.; Huang, F.; Wang, X. Effects of FeO and CaO/Al_2O_3 Ratio in Slag on the Cleanliness of Al-Killed Steel. *Metall. Mater. Trans. B* **2018**, *49*, 3127–3136. [CrossRef]
4. Yang, W.; Wang, X.; Zhang, L.; Shan, Q.; Liu, X. Cleanliness of Low Carbon Aluminum-Killed Steels during Secondary Refining Processes. *Steel Res. Int.* **2013**, *84*, 473–489. [CrossRef]
5. Deng, X.; Ji, C.; Cui, Y.; Tian, Z.; Yin, X.; Shao, X.; Yang, Y.; McLean, A. Formation and evolution of macro inclusions in IF steels during continuous casting. *Ironmak. Steelmak.* **2017**, *44*, 739–749. [CrossRef]
6. Deng, X.; Ji, C.; Dong, W.; Li, L.; Yin, X.; Yang, Y.; McLean, A. Distribution of macro-inclusions in low carbon aluminium-killed steel slabs. *Ironmak. Steelmak.* **2018**, *45*, 592–602. [CrossRef]
7. Yu, H.; Deng, X.; Wang, X.; Ji, C.; Zhu, G. Characteristics of subsurface inclusions in deep-drawing steel slabs at high casting speed. *Metall. Res. Technol.* **2015**, *112*, 608. [CrossRef]
8. Li, L.; Wang, X.; Deng, X.; Wang, X.; Qin, Y.; Ji, C. Application of High Speed Continuous Casting on Low Carbon Conventional Slab in SGJT. *Steel Res. Int.* **2014**, *85*, 1490–1500. [CrossRef]
9. Qin, Y.; Wang, X.; Huang, F.; Chen, B.; Ji, C. Influence of reoxidation by slag and air on inclusions in IF steel. *Metall. Res. Technol.* **2015**, *112*, 405. [CrossRef]
10. Ren, Q.; Zhang, L. Effect of Cerium Content on Inclusions in an Ultra-Low-Carbon Aluminum-Killed Steel. *Metall. Mater. Trans. B-Process Metall. Mater. Process. Sci.* **2020**, *51*, 589–600. [CrossRef]
11. Li, X.; Li, B.; Liu, Z.; Niu, R.; Liu, Q. In-situ Analysis and Numerical Study of Inclusion Distribution in a Vertical-bending Caster. *ISIJ Int.* **2018**, *58*, 2052–2061. [CrossRef]
12. Liu, Z.; Li, B. Effect of vertical length on asymmetric flow and inclusion transport in vertical-bending continuous caster. *Powder Technol.* **2018**, *323*, 403–415. [CrossRef]
13. Liu, Z.; Li, B.; Wu, M.; Xu, G.; Ruan, X.; Ludwig, A. An Experimental Benchmark of Non-metallic Inclusion Distribution Inside a Heavy Continuous-Casting Slab. *Metall. Mater. Trans. A* **2019**, *50*, 1370–1379. [CrossRef]
14. Yamamoto, K.-I.; Yamamura, H.; Suwa, Y. Behavior of Non-metallic Inclusions in Steel during Hot Deformation and the Effects of Deformed Inclusions on Local Ductility. *ISIJ Int.* **2011**, *51*, 1987–1994. [CrossRef]
15. Xu, G.; Jiang, Z.; Li, Y. Formation Mechanism of CaS-Bearing Inclusions and the Rolling Deformation in Al-Killed, Low-Alloy Steel with Ca Treatment. *Metall. Mater. Trans. B* **2016**, *47*, 2411–2420. [CrossRef]
16. Yang, W.; Guo, C.; Zhang, L.; Ling, H.; Li, C. Evolution of Oxide Inclusions in Si-Mn Killed Steels During Hot-Rolling Process. *Metall. Mater. Trans. B* **2017**, *48*, 2717–2730. [CrossRef]
17. Huang, F.; Su, Y.F.; Kuo, J. High-Temperature Deformation Behavior of MnS in 1215MS Steel. *Met. Mater. Int.* **2018**, *24*, 1333–1345. [CrossRef]
18. Zhang, L.; Guo, C.; Yang, W.; Ren, Y.; Ling, H. Deformability of Oxide Inclusions in Tire Cord Steels. *Metall. Mater. Trans. B* **2018**, *49*, 803–811. [CrossRef]
19. Zhou, Q.; Zhang, J.; Yin, Y.; Zhai, M. Characterization of inclusions in axle steel by ingot casting. *Metall. Res. Technol.* **2019**, *116*, 501. [CrossRef]
20. Wang, K.; Jiang, M.; Wang, X.; Wan, W.; Wang, Y. Behavior of Dual-Phase (MnO-SiO_2-Al_2O_3) + (SiO_2) Inclusions in Saw Wire Steels During Hot Rolling and Cold Drawing. *Metall. Mater. Trans. B* **2020**, *51*, 95–101. [CrossRef]
21. Yang, W.; Peng, K.; Zhang, L.; Ren, Q. Deformation and fracture of non-metallic inclusions in steel at different temperatures. *J. Mater. Res. Technol.* **2020**, *9*, 15016–15022. [CrossRef]
22. Niu, K.; Conejo, A.N. Effect of Al_2O_3 on Evolution of Oxide Inclusions in Tire Cord Steel during Hot Rolling. *ISIJ Int.* **2021**, *61*, 2605–2612. [CrossRef]
23. Wang, Y.; Zhang, L.; Ren, Y.; Li, Z.; Slater, C.; Peng, K.; Liu, F.; Zhao, Y. Effect of Thermal History on the Deformation of Non-metallic Inclusions During Plain Strain Compression. *Metall. Mater. Trans. B* **2021**, *52*, 1200–1206. [CrossRef]
24. Wang, Y.; Zhang, L.; Ren, Y.; Li, Z.; Slater, C.; Peng, K.; Liu, F.; Zhao, Y. Effect of compression temperature on deformation of CaO–CaS–Al_2O_3–MgO inclusions in pipeline steel. *J. Mater. Res. Technol.* **2021**, *11*, 1220–1231. [CrossRef]
25. Wang, Y.; Yang, Y.; Dong, Z.; Park, J.H.; Mi, Z.; Mao, X.; Mu, W. Inclusion Engineering in Medium Mn Steels: Effect of Hot-Rolling Process on the Deformation Behaviors of Oxide and Sulfide Inclusions. *Metall. Mater. Trans. B* **2022**, *53*, 2182–2197. [CrossRef]
26. Yang, Y.; Zhan, D.; Qiu, G.; Li, X.; Jiang, Z.; Zhang, H. Inclusion evolution in solid steel during rolling deformation: A review. *J. Mater. Res. Technol.* **2022**, *18*, 5103–5115. [CrossRef]
27. Shu, Q.; You, C.; Alatarvas, T.; Fabritius, T.M.J. Experimental and Modeling Study of Deformability of Glassy CaO-(MnO)-Al_2O_3-SiO_2 Inclusions. *Metals* **2022**, *12*, 522. [CrossRef]
28. Luo, C. Evolution of voids close to an inclusion in hot deformation of metals. *Comput. Mater. Sci.* **2001**, *21*, 360–374. [CrossRef]
29. Luo, C.; Ståhlberg, U. Deformation of inclusions during hot rolling of steels. *J. Mater. Process. Technol.* **2001**, *114*, 87–97. [CrossRef]

30. Luo, C.; Ståhlberg, U. An Alternative Way for Evaluating the Deformation of Mns Inclusions in Hot Rolling of Steel. *Scand. J. Metall.* **2002**, *31*, 184–190. [CrossRef]
31. Ervasti, E.; Ståhlberg, U. Void initiation close to a macro-inclusion during single pass reductions in the hot rolling of steel slabs: A numerical study. *J. Mater. Process. Technol.* **2005**, *170*, 142–150. [CrossRef]
32. Tripathy, P.K.; Das, S.; Jha, M.K.; Singh, J.B.; Kumar, A.M.; Das, A.K. Migration of slab defects during hot rolling. *Ironmak. Steelmak.* **2006**, *33*, 477–483. [CrossRef]
33. Yu, H.; Bi, H.; Liu, X.; Tu, Y. Strain distribution of strips with spherical inclusion during cold rolling. *Trans. Nonferrous Met. Soc. China* **2008**, *18*, 919–924. [CrossRef]
34. Yu, H.; Liu, X.; Li, X. FE analysis of inclusion deformation and crack generation during cold rolling with a transition layer. *Mater. Lett.* **2008**, *62*, 1595–1598. [CrossRef]
35. Yu, H.; Bi, H.; Liu, X.; Chen, L.; Dong, N. Behavior of Inclusions with Weak Adhesion to Strip Matrix during Rolling Using FEM. *J. Mater. Process. Technol.* **2009**, *209*, 4274–4280. [CrossRef]
36. Yu, H.; Liu, X.; Bi, H.; Chen, L. Deformation behavior of inclusions in stainless steel strips during multi-pass cold rolling. *J. Mater. Process. Technol.* **2009**, *209*, 455–461. [CrossRef]
37. Cheng, R.; Zhang, J.; Wang, B. Deformation behavior of MnO13%-$Al_2O_3$18%-$SiO_2$69% inclusion in different steels during hot rolling processes. *Metall. Res. Technol.* **2017**, *114*, 608. [CrossRef]
38. Cheng, R.; Zhang, J.; Wang, B. Formation Mechanism of Voids around Hard Inclusion during Hot Rolling Processes. *High Temp. Mater. Process.* **2018**, *37*, 717–723. [CrossRef]
39. Cheng, R.; Zhang, J.; Wang, B. Deformation Behavior of Inclusion System CaO–Al_2O_3–SiO_2 with Different Compositions During Hot Rolling Processes. *Trans. Indian Inst. Met.* **2018**, *71*, 705–713. [CrossRef]
40. Li, X.; Bao, Y.; Wang, M. Genetic Evolution of Inclusions in Interstitial-Free Steel During the Cold Rolling Processes. *Trans. Indian Inst. Met.* **2018**, *71*, 1067–1072. [CrossRef]
41. Li, X.; Bao, Y.; Wang, M. Peeling defects of cold rolled interstitial-free steel sheet due to inclusion movement. *Ironmak. Steelmak.* **2020**, *47*, 1–5. [CrossRef]
42. Guan, J.; Wang, L.; Zhang, C.; Ma, X. Effects of non-metallic inclusions on the crack propagation in bearing steel. *Tribol. Int.* **2017**, *106*, 123–131. [CrossRef]
43. Gohari, S.; Mouloodi, S.; Mozafari, F.; Alebrahim, R.; Moslemi, N.; Burvill, C.; Badri Albarody, T.M. A new analytical solution for elastic flexure of thick multi-layered composite hybrid plates resting on Winkler elastic foundation in air and water. *Ocean. Eng.* **2021**, *235*, 109372. [CrossRef]
44. Gohari, S.; Sharifi, S.; Burvill, C.; Mouloodi, S.; Izadifar, M.; Thissen, P. Localized failure analysis of internally pressurized laminated ellipsoidal woven GFRP composite domes: Analytical, numerical, and experimental studies. *Arch. Civ. Mech. Eng.* **2019**, *19*, 1235–1250. [CrossRef]
45. Gohari, S.; Mozafari, F.; Moslemi, N.; Mouloodi, S.; Alebrahim, R.; Ahmed, M.; Abdi, B.; Sudin, I.; Burvill, C. Static and dynamic deformation response of smart laminated composite plates induced by inclined piezoelectric actuators. *J. Compos. Mater.* **2022**, *56*, 3269–3293. [CrossRef]
46. Khalid, H.M.; Ojo, S.O.; Weaver, P.M. Inverse differential quadrature method for structural analysis of composite plates. *Comput. Struct.* **2022**, *263*, 106745. [CrossRef]
47. Kabir, H.; Aghdam, M.M. A generalized 2D Bézier-based solution for stress analysis of notched epoxy resin plates reinforced with graphene nanoplatelets. *Thin-Walled Struct.* **2021**, *169*, 108484. [CrossRef]
48. Wang, M.; Bao, Y.P.; Cui, H.; Wu, W.S.; Wu, H.J.; Chen, B.; Ji, C.X.; Zhu, G.S. Surface cleanliness evaluation in Ti stabilised ultralow carbon (Ti-IF) steel. *Ironmak. Steelmak.* **2011**, *38*, 386–390. [CrossRef]
49. Lee, G.-G.; Shin, H.-J.; Thomas, B.G.; Kim, S.-H. Asymmetric Multi-Phase Fluid Flow and Particle Entrapment in A Continuous Casting Mold. *Proc. AISTech* **2008**. Available online: https://www.semanticscholar.org/paper/Asymmetric-Multi-phase-Fluid-Flow-and-Particle-in-a-Lee-Shin/8ed62d6d1348158418504e79569c4ddd3b0ceb3a?p2df (accessed on 10 March 2023).
50. Yin, Y.; Zhang, J. Large eddy simulation of transient transport and entrapment of particle during slab continuous casting. *J. Iron Steel Res. Int.* **2022**, *29*, 247–262. [CrossRef]
51. Liu, Z.; Li, B.; Zhang, L.; Xu, G. Analysis of Transient Transport and Entrapment of Particle in Continuous Casting Mold. *ISIJ Int.* **2014**, *54*, 2324–2333. [CrossRef]
52. Yin, Y.; Zhang, J.; Ma, H.; Zhou, Q. Large Eddy Simulation of Transient Flow, Particle Transport, and Entrapment in Slab Mold with Double-Ruler Electromagnetic Braking. *Steel Res. Int.* **2021**, *92*, 2000582. [CrossRef]